THE ASTROPHYSICAL JOURNAL, 447:191–203, 1995 July 1

STELLAR VARIABILITY IN THE CENTRAL POPULATIONS OF 47 TUCANAE FROM WF/PC OBSERVATIONS WITH THE *HUBBLE SPACE TELESCOPE*. I. PROJECT OVERVIEW, REDUCTION TECHNIQUES, AND FIRST RESULTS[1]

RONALD L. GILLILAND, PETER D. EDMONDS, LARRY PETRO, ABHIJIT SAHA, AND MICHAEL M. SHARA
Space Telescope Science Institute,[2] 3700 San Martin Drive, Baltimore, MD 21218;
gillil@stsci.edu, pedmonds@stsci.edu, petro@stsci.edu, saha@stsci.edu, mshara@stsci.edu
Received 1994 December 5; accepted 1995 January 10

ABSTRACT

Stars in the central region of the dense globular cluster 47 Tucanae were monitored for variability using time-resolved photometry from 99 *Hubble Space Telescope* Planetary Camera exposures of 1000 s in the F336W (*U*) filter. The observations were obtained while 47 Tuc was in the continuous viewing zone (CVZ) of *HST*. This data set provides an unparalleled sensitivity for quantification of stellar variability: (1) in the blue straggler population, δ Scuti oscillations would provide important constraints on these enigmatic stars; (2) studies of cataclysmic variables detectable through dwarf novae outbursts or orbital modulation are of interest in testing formation theories; (3) eclipsing binaries and W UMa systems are of fundamental interest for cluster dynamics considerations. In this paper the unique data analysis challenges posed in following some 20,000 (undersampled PSF cores with extended spherical aberration induced halos) stars with near-Poisson limited precisions given the complications of image motion and a high rate of cosmic rays are addressed in detail. Examples of the oscillating blue stragglers, eclipsing binaries, and near-contact binary systems detected in this project are discussed.

Subject headings: binaries: eclipsing — blue stragglers — δ Scuti — globular clusters: individual (47 Tucanae) — methods: data analysis — novae, cataclysmic variables

1. INTRODUCTION

The cores of globular clusters, and 47 Tucanae in particular, provide a prolific breeding environment for exotic objects. Blue stragglers (Paresce et al. 1991; Guhathakurta et al. 1992; De Marchi, Paresce, & Ferraro 1993), X-ray binaries (Hertz & Grindlay 1983), and millisecond pulsars (Manchester et al. 1991) exist in overabundance by orders of magnitude in the core of 47 Tuc relative to field populations. The tight central concentration of blue stragglers in 47 Tuc (similar objects were not seen off-center in the Hesser et al. 1987 study) suggests that these are more massive objects than the mixture of single giants, subgiants, and dwarfs. The larger masses suggest either tight binaries (soft binaries would be quickly disrupted in the dense 47 Tuc core) or single stars with significantly higher than main-sequence turnoff masses. It is a matter of considerable importance to the dynamical evolution of globular clusters, whether or not the existing population of blue stragglers are primarily single stars or binaries. Monitoring these objects for variability of δ Scuti (often called SX Phe for Population II stars) type or W UMa modulation provides important clues to the status (single or binary) of the blue stragglers. In the data reported here, we find that variability is remarkably common with the 47 Tuc blue stragglers and that both δ Scuti and contact binary systems are represented.

Stellar densities in the core of 47 Tucanae are high enough for predictions of a strongly interacting population with tidal captures (Fabian, Pringle, & Rees 1975), binary disruptions (Hut, McMillan, & Romani 1992), and stellar collisions and mergers (Hills & Day 1976). A proper qualitative understanding of dynamical evolution of clusters will follow only after the formation, evolution, and destruction of close binaries are accounted for (Hut et al. 1992), since the energies of just a few tens of tight binaries can rival the binding energy of the cluster. The abundance of exotic objects in the 47 Tucanae core emphasizes that extreme conditions leading to strong interactions do exist.

Although some useful surveys for variability in globular cluster cores have been done from the ground (see, e.g., Mateo et al. 1990; Mateo 1993; Yan & Mateo 1994), only with the high spatial resolution of *HST* imaging is it possible to probe for variables in the core of 47 Tucanae and like clusters of high stellar density. An early success is the monitoring of the core of NGC 6752 continuously for 7 hr (Shara et al. 1995a) in a search for contact and cataclysmic binaries.

The data discussed below are unique in several ways:

1. Our observing program was the first to utilize the continuous viewing zone (CVZ) of *HST* for a substantial science program—its execution has served to "open up" the CVZ to routine use to the benefit of both general efficiency and special capabilities for intensive time-series observations.

2. A nearly continuous sequence of CCD images over a 38.5 hr time span allows engineering analysis on topics such as *HST* guiding stability, temporal variability in the background rate of cosmic rays, and sky brightness variations throughout *HST* orbits that had not been previously quantified.

3. The resulting time series photometry on some 20,000 stars with well-understood noise characteristics allows for an unprecedented survey for variable stars in a dense globular cluster core.

[1] Based on observations with the NASA/ESA Hubble Space Telescope obtained at the Space Telescope Science Institute, which is operated by Association of Universities for Research in Astronomy, Incorporated, under NASA contract NAS 5-26555.

[2] Operated by the Association of Universities for Research in Astronomy, Inc., under contract with the National Aeronautics and Space Administration.

4. This sequence of 99 exposures was the most substantial generated by the WF/PC in its 3.5 yr on orbit.

The science goals of this project have been touched on in the above introduction. Briefly summarized, we proposed to obtain a definitive survey of the central 47 Tuc stellar population for both single star and binary system variability. Detected variables (and limits to detections) would provide material for astrophysical considerations related to the structure of blue stragglers, the formation mechanisms of cataclysmic variables (CVs) active in globular cluster cores, and the importance of tight binary systems for the dynamical evolution of globular cluster cores. Results for these goals will be detailed in a series of papers in preparation: Shara et al. (1995b) on cataclysmic variables, Gilliland et al. (1995) on the blue stragglers and δ Scuti oscillations, and Edmonds et al. (1995) on W UMa and other binary systems.

Derivation of the best possible time series of differential photometry was the primary technical goal in this project. Fulfillment of this involved development of new observational and data analysis methods—discussions of these are considered fully in §§ 2 and 3 of this paper. An overview of time series properties for both bright objects and faint stars in our sample will appear in § 4; although astrophysical interpretations will be deferred to further papers in this series, samples of both the variable star light curves provided by the WF/PC on *HST*, and examples of common artifacts are shown. Section 5 provides a summary, a look to the future for what this project will have accomplished, and a discussion of where the new frontier is for related future observations.

2. OBSERVATIONS

2.1. *The Basic Data Set*

Observations with the planetary camera of WF/PC on *HST* were obtained in a time series mode from 1993 September 4, UT 20:43 through 1993 September 6, UT 11:30. A total of 99 exposures through F336W during the above interval were obtained; 91 of these had an exposure time of 1000 s, and an additional 8 had exposures of 900 s—the latter exposure time difference to facilitate scheduling in tight windows. The rootnames corresponding to the F336W time series are spanned by w1kx0101t through w1kx0308t. In the next *HST* orbit an additional four frames (w1kx040[1–8]t) in each of F439W and F555W were acquired at staggered exposure times of 20, 35, 70, 160 s (F439W) and 8, 16, 30, and 60 s (F555W) to provide color information. In the 1000 s F336W frames none of the bright stars reached saturation. The short exposures in *B* and *V* provide color information on the bright program stars, while the longer single exposures saturate the bright stars but provide color information on the faintest objects that can be followed in the *U*-band time series.

2.2. *Continuous Viewing Zone Observations*

During the 38.5 hr period of the F336W time-series observations the duty cycle (ratio of shutter open and observing to total "wall clock" time) exceeded 70%; *HST* observations can be very efficient. The 70% duty cycle was maintained even with allowance for instrument overheads, lost periods due to South Atlantic Anomaly passages, and the need for frequent tape recorder dumps. Normal *HST* observations suffer an occultation by Earth for a substantial part of the 96.3 minute *HST* orbit which forces a much lower overall observing efficiency. Since this program not only was the first to substantially benefit from CVZ utilization for a unique science observation, but also contributed in a fundamental way to opening up *HST* operations for CVZ use, a few words on this basic observational method are in order.

Due to minimum energy launch constraints to reach a long-lived, but serviceable, orbit the *HST* was launched on the shuttle due east into an orbit inclined 28°.5 to the equator. The pole of *HST*'s orbit is therefore at a declination of $\pm 61°.5$. Precession of the *HST* orbital plane occurs on a 56 day period, thus sweeping the *HST* orbital poles over all right ascensions at the 61°.5 declination. With a (1993) altitude for *HST*'s orbit ($a = 580$ km) simple trigonometry shows that the half-angle blocked geometrically from view by Earth is given by $\sin(\theta) = R/(R + a)$ implying a value for θ of 66°.4 where R equals the Earth radius. The Earth-limb distance with *HST* viewing its own orbital pole is $90° - 66°.4 = 23°.6$, since this exceeds the limb-angle avoidance (minimum distance between *HST* and the Earth limb before expected scattered light exceeds useful limits) constraint for observations the pole and adjacent area on the sky comprise a CVZ. The minimum Earth-limb angles are 20° from the bright limb (the FGSs can support guiding to 15°.5) and 7°.6 from a dark limb.

As now implemented with *HST* the CVZ extends over $54° \leq |\delta| \leq 77°$ (these limits are not symmetric about the orbital pole since the Sun is always on the small declination side and its avoidance serves to limit the small declination extent) and single passages through the CVZ can be as long as 6.5 days during which time *real* observing efficiency can approach 80%–90%. Hundreds of hours per year of *HST* observing have effectively been added by better utilization of the CVZ.

2.3. *Characteristics of Data Frames*

The four PC CCDs in WF/PC span a nearly contiguous area on the sky of 66 arcsec^2. We positioned the nominal center of 47 Tuc about 10″ from the apex of PC6. With many thousands of stars imaged onto each CCD frame and spherical aberration halos on each covering a disk some 5″ wide, the data has a false sky background dominated by the overlapping halos in the crowded stellar field. (The real sky level will be addressed in § 3.) The general background level varies from some 5 ADU (7–8 e^-/DN) in regions of lowest stellar density to typically 30 ADU near the cluster center. This intrinsic background is large enough to ameliorate the WF/PC low-intensity charge transfer problem; we disabled the preflash option for these data frames.

The imaging performance of *HST* with WF/PC is described by Burrows et al. (1991). At 336 nm the PC pixels at 0″.043 undersample the stellar image cores that contain some 15% of the total energy. Although spherical aberration creates large, low-intensity halos, the exquisite spatial resolution that for the most part remains quite stable with time allows some 5000 stars to be well separated on each of the 800 × 800 CCDs. Figure 1 (Plate 7) shows a 400 × 400 pixel region from PC6 (7% of total imaged area) that is centered on the core of 47 Tuc.

For the purposes of deriving differential time series photometry, some WF/PC data characteristics problematic for absolute photometry do not trouble us, e.g., the spatial variation of the PSF is not a problem. Of greater significance for time series work is defining what external (to the stellar intensities) data characteristics change frame to frame. We may

PLATE 7

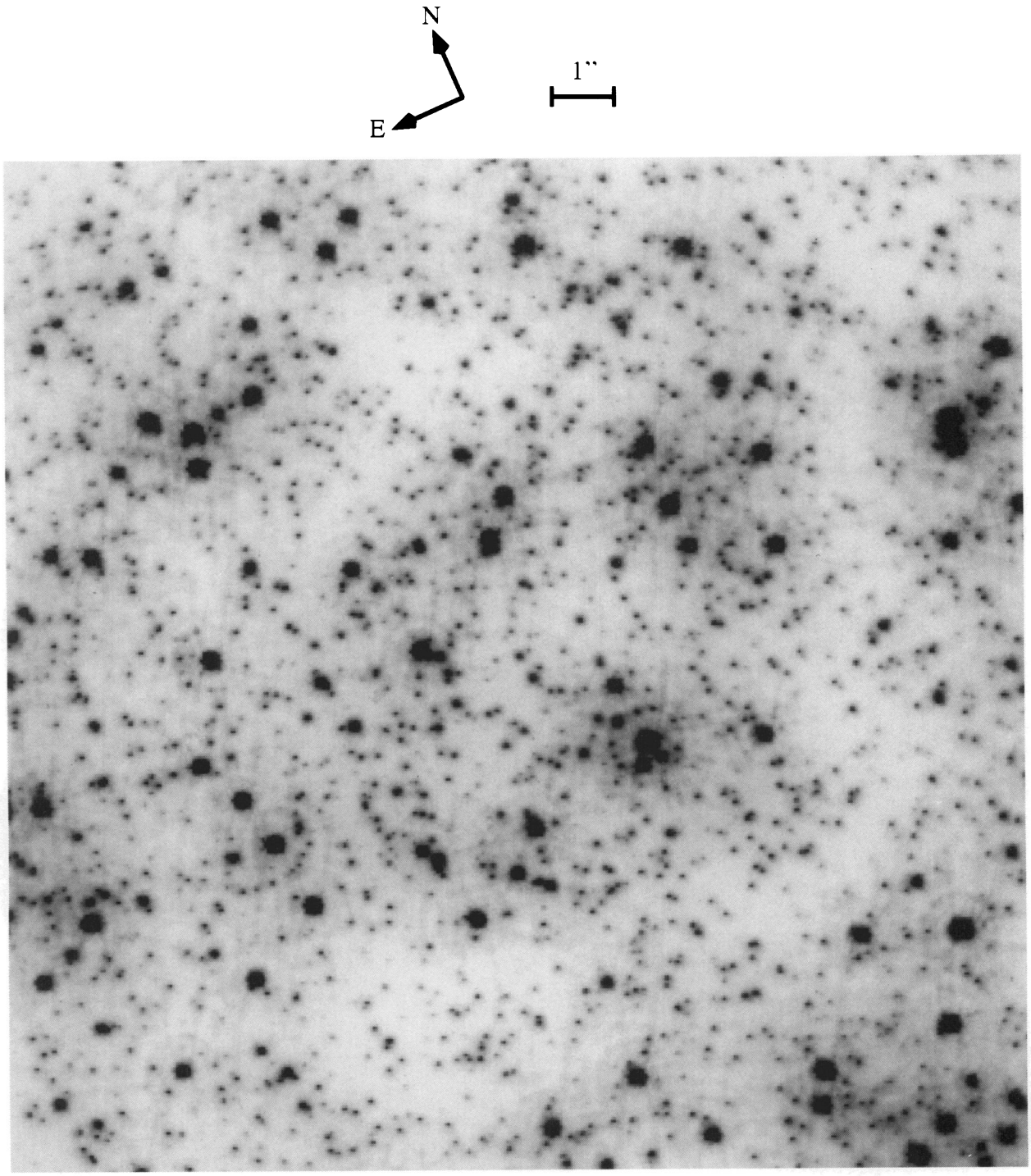

FIG. 1.—A 400 × 400 pixel region from PC6 at the center of 47 Tucanae. This is a mean (see text for details) of 99 F336W exposures of 1000s.

expect that some dominant problems for ground-based time series work, e.g., atmospheric transparency variations, scintillation, and seeing fluctuations, will not be present. However, minor fluctuations of telescope focus ("breathing") due to changing thermal loads over the *HST* orbit, as well as small guiding errors, may exist.

The magnitude of guiding errors will to a large extent determine the difficulty of several data reduction and stellar image intensity analysis steps. If the guiding error, i.e., the variation of the position of the image relative to the CCD pixels, remains very small, say $\lesssim 0.1$ pixel, then cosmic rays could be trivially eliminated by searching for multi-σ positive deviations from time series of individual pixels, and intensities could be extracted over the 99 time series frames by following aperture sums fixed in pixel space. Figure 2 shows the time series of stellar position versus CCD coordinate offsets for PC8; traces for the other CCDs differ only in detail (with appropriate multiple of 90° rotations imposed such that x, y maintains a common relationship to celestial coordinates). Clearly the *HST* guiding, while excellent by normal standards, did not maintain stability at the 0.1 PC pixel level that would simplify our data analysis. Figure 3 documents the effect of image motion for the intensity detected by a pixel ($i, j = 397, 299$ on PC 8) on the edge of a stellar PSF core. The *HST* orbit tracking error can modulate individual pixel intensities by 30%–40% while the long-term drift of ~ 1 PC pixel can modulate pixel intensities by 300%–400%. At $3000e^-$ the expected Poisson fluctuation is 1.8%, and the pixel-to-pixel flat-field fluctuations should be comparably small. With undersampled images, even small registration errors can produce pixel intensity changes at a level orders of magnitude larger than Poisson fluctuations. In this and similar data sets image motion greater than ~ 0.01 pixel will in fact be substantial enough to mask easy detection of weak cosmic-ray events that if left untreated would contribute significantly to the overall error budget for stellar photometry. (The "cosmic-ray" bar in Fig. 3 has been given a length of 453 electrons to illustrate the amplitude of the average cosmic-ray hit; the position of this bar in the diagram has no particular significance.) Other pixels located at symmetric positions with respect to the PSF core will show equal and opposite responses to the tracking changes, such that the sum over a reasonably sized aperture will yield a constant (to expected Poisson and readout noise variations—for bright stars these sum to $< 1\%$) signal in time.

We will show below that on average a pixel suffers 1.2 hits by cosmic rays at an average energy (for those detected) of $453e^-$ during the 98,200 s (plus readout time) of time series integrations. If we assume stellar intensities are derived from $r = 2$ pixel apertures, then a star would suffer $1.2\pi r^2 = 15.1$ cosmic-ray hits over 99 frames; at $r = 3$ pixels this increases to 33.9 hits on average. For the fairly bright star used for Figure 3 the aperture intensity is about 3×10^4, yielding expected Poisson fluctuations of $173e^-$. Therefore, if aperture sums over $r = 3$ (28 pixels) are used, there would be (statistically) 34 cosmic-ray hits averaging 2.6 σ over 99 time series points. Even for bright stars, cosmic rays, unless effectively removed from the data, will contribute strongly to the error budget. The technical challenge, discussed at length in the next section, is how to elimi-

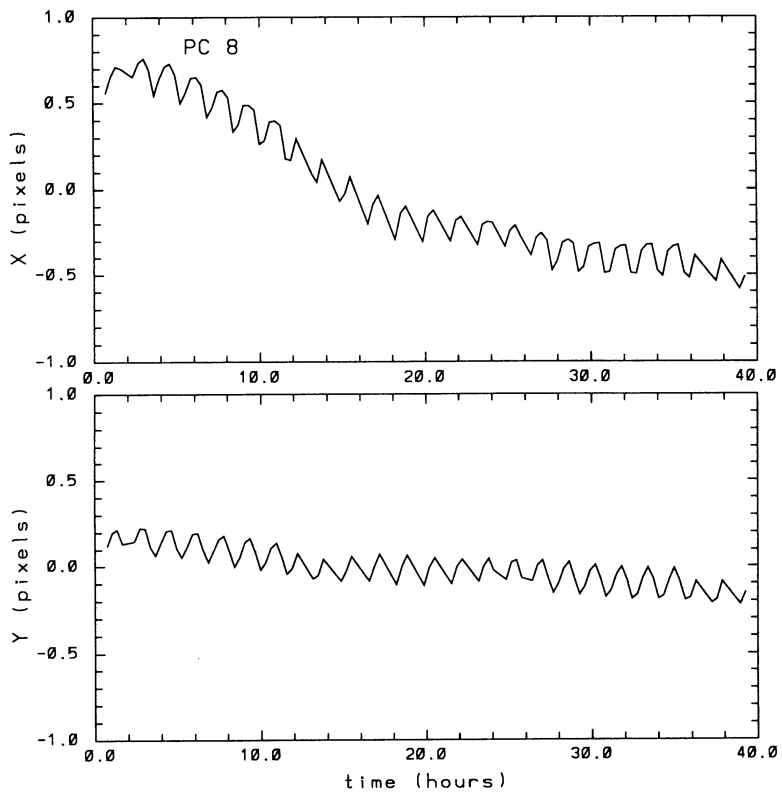

FIG. 2.—Relative offsets of image and CCD coordinates over the primary time series of 99 frames. The scale is in pixels (= 0.″043), and for convenience all plots in this paper will be against time in hours. (The first data frame has a midpoint time of HJD 2, 449, 234.85748.) This is for PC8. Both orbital modulation and a long-term drift are evident.

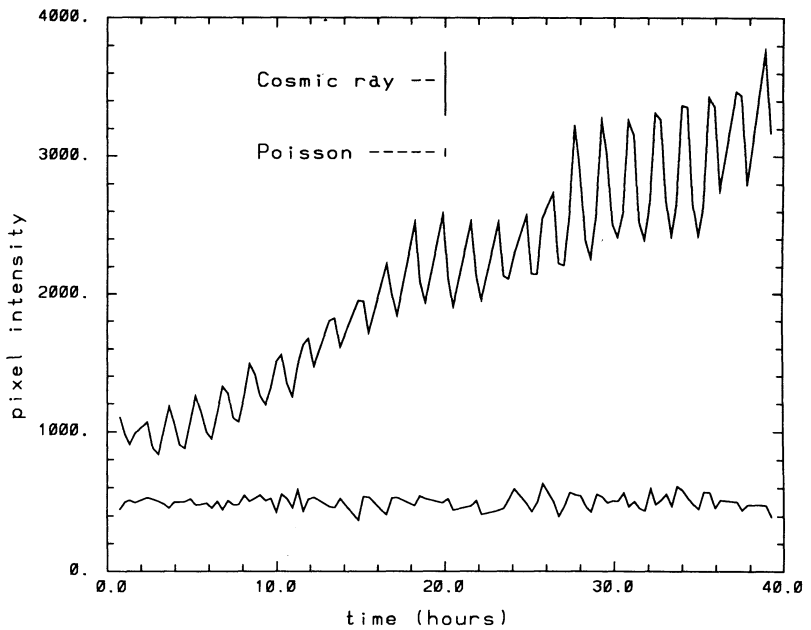

FIG. 3.—An illustration of intensity variations (*upper curve*) through the time series for a specific pixel on the edge of a stellar PSF core. Intensity units are in electrons. Vertical bars show magnitudes of Poisson fluctuations (at $3000e^-$) and illustrate the average energy of detected cosmic-ray events. The lower curve shows the residuals (arbitrary offset of +500 for plotting) between the observed and modeled intensity variation (see eq. [3] and associated discussion).

nate cosmic rays which are multi-σ perturbations based on Poisson statistics when image motion creates much larger frame-to-frame variations for a given pixel.

3. ANALYSIS TECHNIQUES

3.1. *The Basics*

We have concentrated our efforts on calibration, reduction, and analysis steps necessary for obtaining optimal differential time-series photometry. Here differential implies only that we are not much concerned with whether the mean level of intensity for one star relative to another is correctly extracted. If we make a mean intensity error at the 10% level between stars, this is fine and doubtless occurs, since we do not try to account for low–spatial frequency errors in flat fields, or for the influence of a spatially variant PSF. If the intensity of two stars supports 1% precision, we are, however, greatly concerned that the same relative error between two stars be made such that the differential time series show only 1% fluctuations. For these purposes the standard STScI supplied pipeline reductions work well. We have applied a new flat field (cc1d1031w.r6h) derived from nearly contemporaneous Earth-flats for F336W but have otherwise adopted the pipeline calibrated data.

To simplify considerations of image motion we have rotated all CCDs by multiples of 90° (with PC8 as standard) to roughly align x, y coordinates. We have also multiplied all calibrated data values by 8.0, thus roughly transforming to electrons (at this stage the data can be stored as 2 byte integers without loss of precision) before performing additional steps.

3.2. *Robust Cosmic-Ray Elimination*

Figure 3 illustrated a problem for simple cosmic-ray removal—image motion, coupled with undersampled stellar PSFs, creates frame-to-frame fluctuations for many pixels large compared to the events that need to be eliminated. For a pixel that "sees" only sky or is in a low-gradient region of a stellar PSF, simple σ-clipping would work well (see, e.g., Windhorst et al. 1994 for removal of cosmic rays from "stacked" WFC images of a field with little intrinsic high spatial frequency structure.) Since we are interested primarily in the regions with high spatial frequencies (undersampled stellar PSF cores) and our data show significant image motion, *we directly face the problem of eliminating cosmic rays from a signal with large intrinsic modulation.*

In Figure 2 we illustrated the x, y position changes of a single bright isolated star relative to CCD coordinates. For each of the four CCDs we have performed PSF fitting (see § 3.6) to 25 bright, isolated stars well distributed over the full field of view. We have found that a full plate solution mapping sky coordinates to CCD pixels requires time variable zero points and scale factors for both x and y:

$$\delta x_{i,j}(t) = x_0(t) + x_{i,j} \times \text{scale}_X(t) \quad (1)$$

$$\delta y_{i,j}(t) = y_0(t) + y_{i,j} \times \text{scale}_Y(t) , \quad (2)$$

where the $\delta x_{i,j}$ and $\delta y_{i,j}$ are relative offsets for a specified pixel, x_0, y_0 represent bulk translations, and scale_X, scale_Y are changes of apparent plate scale. These four-parameter (least-squares) fits to 50 x and y positions per CCD frame are sufficient to yield stable solutions with mean position errors of only 0.024 pixels (x and y combined) rms, or solutions that are good to 0".001. Allowance for a possible time-variable rotation of sky and CCD coordinates does not result in a better solution. Figure 4 shows the derived variation of plate scale for PC8, an effect smaller by a factor of 10 than the translations shown in Figure 2, but nonetheless quite significant. (The cause of significantly different variations of apparent scale in x and y is not known.) The stellar positions used for equations (1) and (2) are derived iteratively after elimination of cosmic rays; in the first pass with cosmic rays affecting the fits, the residuals are much larger.

It is sufficient to consider a single pixel (say $i = 397, j = 299$ from PC8 as shown in Fig. 3) over the 99 time series frames to understand our cosmic-ray elimination scheme. Equations (1)

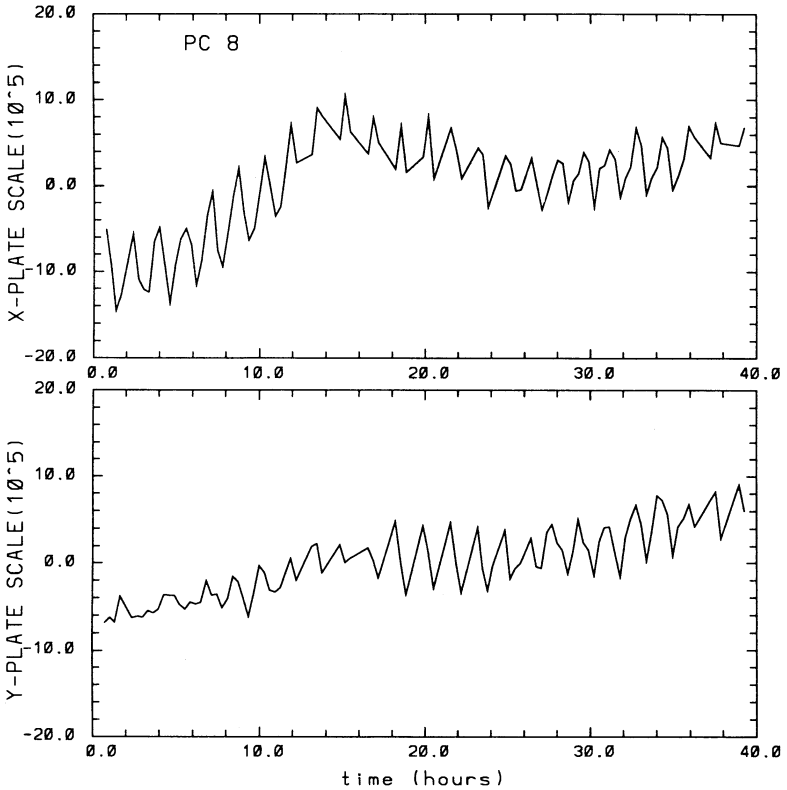

FIG. 4.—Plate scale variations over time for PC8 (see eqs. [1] and [2])

and (2) yield a time series of $\delta x(t)$, $\delta y(t)$ for a pixel in question and $I(t)$ the apparent intensity is readily available. We assume that the non-Poissonian fluctuations in intensity for a given pixel can be expressed as a simple function of the x and y offsets:

$$I_{i,j}(t) = f[\delta x_{i,j}(t), \delta y_{i,j}(t)] . \quad (3)$$

We have settled on a choice for f of up to a third-order Legendre polynomial in both x and y as required to yield a good model intensity. In setting up the Legendre fit, the δx, δy are remapped to fall within a unit domain (see also discussion in § 3.4) as required for the orthogonal function fitting. The least-squares polynomial fits are performed iteratively after eliminating cosmic rays (σ-clipping) as multi-σ positive deviations above the model intensity value. Only the orthogonal polynomial coefficients determined to be statistically significant (coefficient value greater than 2.5 times the mean error) are retained in a final iteration. Thus most pixels that are far from stellar cores are represented just by a constant value; pixel intensities like the one chosen for Figure 3 that show great sensitivity to position retain all seven (cross-terms in x and y have not been used; the highly correlated δx and δy allow excellent results with just the pure x and y terms) coefficients for the intensity model.

The σ-clipping above a modeled intensity assumes the maximum of expected fluctuations based on readout noise plus Poisson statistics of the mean intensity and the actual rms about the fit. Thus the threshold for eliminating cosmic rays will be raised for cases in which the star is intrinsically variable or simply for which the model does not work well. We have adopted a final σ-clipping value of 2.7 σ (one-sided only).

The efficacy of equation (3) in representing image motion–driven intensity fluctuations is demonstrated in Figure 3 in which the difference between the data and model fit is shown (offset vertically at the bottom). The rms difference is 48.8, i.e., the expected Poisson fluctuation level at an intensity of $2381e^-$—a good approximation to the mean level of the data series. Therefore one is effectively searching for cosmic-ray–induced deviations (average size as indicated) added to a time series vector with essentially Poisson deviations.

We have of course verified via direct testing that the cosmic-ray elimination algorithm does not adversely impact our results by "clipping" high points on stars that are of intrinsic interest due to stellar variability. For δ Scuti– or W UMa–like variations, or any light curve in which the intrinsic variations contribute strongly to an overall increase of time series variance, the adopted algorithm is safe. We would "clip" and ignore isolated positive excursions, e.g., flare-like events—since such objects are not of primary interest to us, this seems a small price to pay for a robust elimination of cosmic rays. Eclipses are retained, since only positive deviations are eliminated. Time series for pixels associated with variable stars have a higher threshold for cosmic-ray elimination; therefore the resulting stellar intensity time series will retain a higher than typical level of noise from undetected cosmic-ray events (this does not present a problem, however).

When a pixel value is flagged as affected by a cosmic ray, its value is replaced by interpolation from its nearest neighbors in time (which were not affected by a cosmic ray) and adjusted for the relative intensity difference based on the intensity model and "known" x, y positions. This assures that spurious points are not introduced into a variable star light curve as would

happen if the time series mean were used for the replacement. The difference between the original data value and the replacement is stored for separate analysis of the cosmic-ray distributions.

The record of cosmic rays (we operate only at the pixel level and do not group spatially contiguous eliminated points into events) detected is of intrinsic interest, since it shows large (and at least to us) unexpected modulation characteristics. Figure 5 shows the temporal variation in number of pixels flagged per frame (sum over 750 × 750 image area on each of the four CCDs) as cosmic rays. The modulation over *HST* orbits is in excess of a factor of 2. Since the integration is generally 1000 s (plus about 50 s for readout overhead and waits for major frame boundaries on 1 minute intervals during which cosmic rays are still integrated) on an ~5800 s orbit the real modulation is damped slightly. A few peaks in Figure 5 have been labeled "m"—for magnetic, and a few have been marked "o"—for orbital. The largest peaks (the "o's") occur in perfect lockstep with the *HST* orbit with the peak occurring in the middle of orbital day (i.e., when *HST* is nearest the subsolar point, or half-way between terminator crossings on the day side). (Perhaps the result of a lower altitude for the radiation belts due to a Sunward compression of Earth's magnetic field.) The smaller "m" peaks follow a different period; one can trace these peaks merging into the shoulders of the orbital peaks smoothly on either side of their centered appearance. The "m" cosmic-ray component loses one beat in 24 hr compared to the *HST* orbit modulation and is therefore interpreted as arising from geomagnetic modulation. (The period from about 14 to 23 hr is impacted by SAA crossings during which data was not obtained.)

We have also examined the number of cosmic rays per factor of two energy bins from 2^6 to 2^{15} deposited electrons per pixel. The small number of events that resulted in detector saturation are counted in the 2^{15} bin. Table 1 summarizes the overall cosmic-ray energy dependence (each bin extends ± 0.5 from the integral exponent center). The component of cosmic rays modulated directly by Earth's magnetic field strengthens relative to the "o" component at higher energies; at a level of 2^{11} e^- per detection the "m" peaks become as high as the direct orbital modulation peaks, but this difference in apparent energy distribution remains subtle. Close inspection of several frames dominated by events from either the "o" or "m" modulation peak times showed no apparent difference in event-track morphology (see Fig. 1*c* of Windhorst et al. 1994 for an illustration of cosmic-ray events).

TABLE 1

COSMIC-RAY ENERGY DISTRIBUTION

$\log_2 e^-$	Number per Frame
15.....	7
14.....	12
13.....	41
12.....	111
11.....	283
10.....	705
9.....	1139
8.....	1199
7.....	1477
6.....	1561
5.....	307

Realizing that elimination of cosmic rays in fields dominated by undersampled stellar images is a complicated process, we separately computed cosmic-ray statistics from the CCD regions within pyramid shadows (active regions on WF/PC CCDs not illuminated by the relay optics). The distribution in the shadows in both time and energy dependence showed a nearly identical distribution to that in Figure 5 and Table 1; the modulation of cosmic rays is real and not an artifact of strong *x*, *y* image motion and subsequent data analysis.

The total number of detected cosmic rays averages ~1.2 per pixel over the 99 time series frames. We compiled how many pixels out of the full four CCD set were hit by 0, 1, 2, ..., 9 events and verified that this was well represented by the expected Poisson distribution. (About 30% of pixels experi-

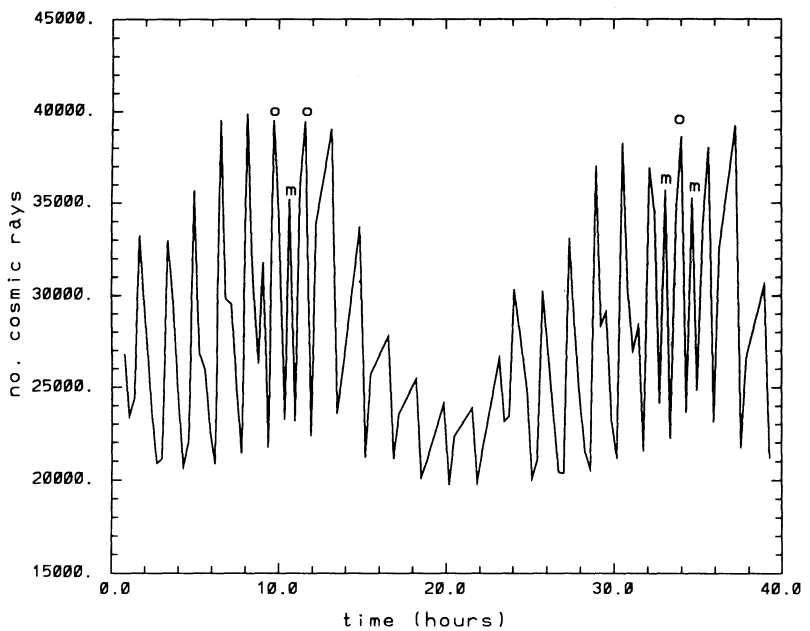

FIG. 5.—Number of cosmic ray (pixels) detected over all four CCDs per frame over time. Peaks labeled "o" and "m" are discussed in the text and show modulation at different frequencies.

enced no hits, 36% one hit, ..., 0.59% five hits, and only four pixels had as many as nine events over the time series.)

We have carefully examined summed frames of the cosmic rays, movies of the eliminated cosmic rays, and the spatial distribution of number of events per pixel. All quality checks suggest that the cosmic rays have been eliminated robustly. Except for the obvious increase of threshold in regions of high intrinsic Poisson fluctuations, we do not believe that the eliminated cosmic rays "know about" the presence of undersampled stellar images and significant frame-to-frame image motion. We will briefly return to a consideration of the temporal variation of cosmic rays in § 3.5.

3.3. *Hot Pixel Elimination*

Each of the four CCDs shows motion in the x-coordinate of $\sim \pm 0.5$ pixels. By evaluating the Legendre polynomial intensity models (eq. [3]) at ± 0.5 in x and comparing the results symmetrically with a shift of i index by one, it is possible to separate CCD coordinate–based defects from real image structure. Although not of great significance for this project, some 1523 hot and dead (this test was done in a two-sided mode) pixels were identified and corrected for in a second iteration on the data reductions.

3.4. *Oversampled Mean Image, χ^2 Maps*

Although not planned for, our data set is effectively dithered by (depending on the chip and position) ± 0.6–0.8 pixels in x and ± 0.1–0.3 pixels in y. Our method of cosmic-ray elimination relied on creating a precise model of subpixel shift intensity modulation. With this in hand it is trivial to evaluate the Legendre polynomial model at all values of $x = \pm 0.25$, $y = \pm 0.25$ for any pixel i, j to create an image with well-posed factor of 2 oversampling. [The realized dithering for this data is correlated in x and y as shown in Fig. 2. Offsets of (x, y) of $(+0.25, +0.25)$ and $(-0.25, -0.25)$ are within the band sampled by the motion. The cross-diagonal offsets are, however, not sampled, and therefore evaluation at these values involves an extrapolation with a resultant increase of noise. The oversampled images shown in (Fig. 6 [Pl. 8] (*lower panel*) are based upon evaluations at (x, y) offsets of $(+0.75, +0.25)$ from pixel $(i-1, j)$ substituting for $(-0.25, +0.25)$ and $(-0.75, -0.25)$ from $(i+1, j)$ substituting for $(+0.25, -0.25)$ in the pixel i, j oversampling. These off-diagonal substitutions from neighboring pixels in the x-direction are possible because the effective dithering in x is greater than 1 pixel. This subtlety is not relevant to intensity modeling for cosmic-ray elimination purposes, since for this the functions are evaluated only within the directly sampled band of motion. An observation intended to support oversampling through dithering should of course utilize offsets that directly sample the desired evaluation points.] Figure 6 compares a (time series mean) region (*upper panel*) of PC5 evaluated at pixel centers (the Legendre zero points) and at 0.5 pixel oversampling. Real resolution is clearly recovered by the dithering and oversampling. (Note that we are not showing, and do not consider, the smearing that would follow from a mere averaging of shifted images. The top panels in Figure 6 show the best resolution possible with individual, or a series of perfectly aligned images. The lower panels show a reconstruction making use of true subpixel information.) The Legendre model coefficients allow evaluation of mean intensities at arbitrary pixel positions and may be used for building full image mosaics of convenient size, e.g., the ~ 1550 contiguous pixels may be mosaiced into a 2048 image with oversampling of $\sim 32\%$ linearly.

A by-product of the cosmic-ray elimination process is a χ^2 map, i.e., an image showing a pixel-by-pixel ratio of realized scatter about the Legendre intensity model (eq. [3]) and that expected from readout noise and mean–pixel intensity Poisson noise. The χ^2 maps generally average near unity in regions away from stellar cores, increasing to typical values of ~ 1.5–2.0 at bright stars. We therefore do not on average do a perfect job at modeling image motion–induced intensity modulations but note from inspection of Figure 3 that pixel time series at the edge of bright stars would experience fluctuations up to χ^2 of 100–1000 without the detailed modeling of eq. (3). The largest amplitude variable stars detected in this project appear clearly in the χ^2 maps, but examination of these maps is not a sensitive variable star detection technique (a star with a single low-amplitude coherent oscillation mode can be easily detected as variable with Fourier-based search techniques, yet have the overall time-series variance perturbed very little).

3.5. *Time-modulated Sky Definition*

Our 38.5 hr of time-series observations on 47 Tuc filled a full CVZ passage—defined to be that period of time during which *HST* does not violate Earth-limb avoidance angles. Therefore some of our observations occurred very near the constraining angles. It is of general interest to thoroughly qualifying the continuous viewing zone of *HST* for further use to report on sky brightness variations. We will show that the sky as seen by *HST* remains essentially nonexistent for 1000 s exposures with F336W.

Defining sky in these crowded fields with overlapping spherical aberration halos is problematic. We will assume the instrument response is stable (to be demonstrated via Fig. 9), and we can show that the influence of variable stars on total counts within a data frame is negligible. Figure 7 shows a derived level of sky fluctuations (arbitrary zero point) assuming that variations in the total counts frame-to-frame (after cosmic-ray elimination) follow simply from changes in the background sky level. The variations in Figure 7 are very similar to those appearing in Figure 5—the fluctuating sky seems to track the cosmic-ray modulation. That some part of apparent sky should arise from, and therefore correlate well with, the cosmic rays is expected. Our sensitivity to cosmic rays, especially those at the lower energies, is decreased in the neighborhood of stars. For example, the pixel detailed in Figure 3 would show evidence for cosmic rays only above energies of $\sim 2.7 \times 48.8 = 132e^-$; most pixels provide lower Poisson limits and the overall bulk of detected cosmic rays (by number) are at energies below this level. The peaks labeled "m" in Figure 5 are present at relatively lower amplitudes in Figure 7—consistent with a preference for missing low-energy events and the already noted relative energy dependence of the two modulated peak sets. We may estimate a lower limit to the number of missed cosmic rays within the illuminated image region by comparison with the (appropriately scaled by area) number detected within the pyramid shadows. Table 1 shows the number of pixels flagged per CCD as cosmic rays (area of 750×750 in primary imaging region) as a function of energy. The contribution of missed cosmic rays in the imaging area may be estimated by extrapolating from the numbers detected at energies of 64 or $128e^-$ down to a cutoff of $1e^-$, summing the excess and normalizing to the pixel area. We do not have a robust estimate of expected frequencies of very low energy

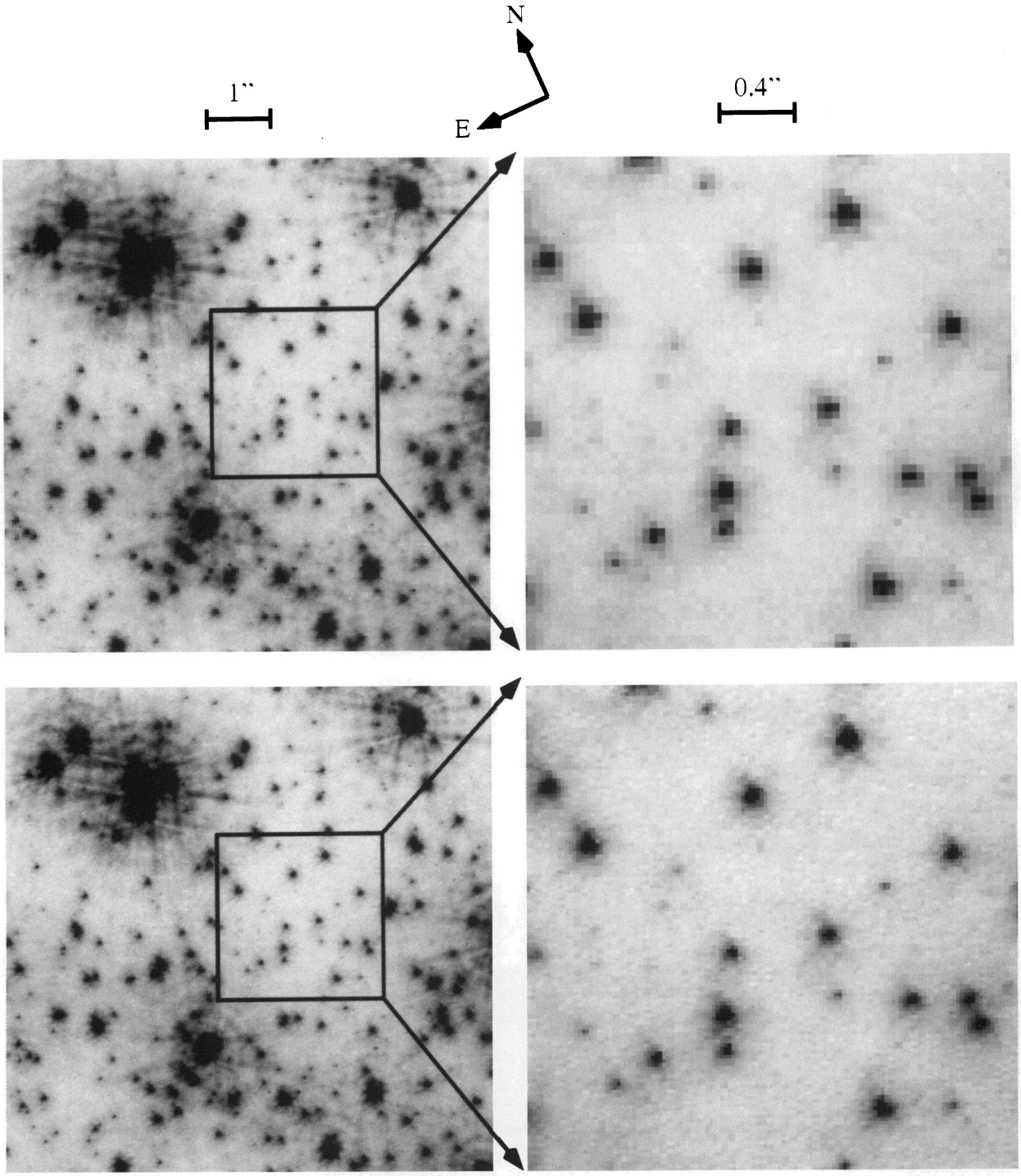

FIG. 6.—The left-hand boxes show a comparison of 195 × 195 pixel regions on PC5 in which the mean of 99 F336W exposures (*top*) is compared with the same (*bottom*) after invoking oversampling by a factor of 2 as described in the text. The boxes on the right-hand side show details on 65 × 65 pixel areas as indicated. With proper subsampling the PSFs are sharper and fainter objects are detectable.

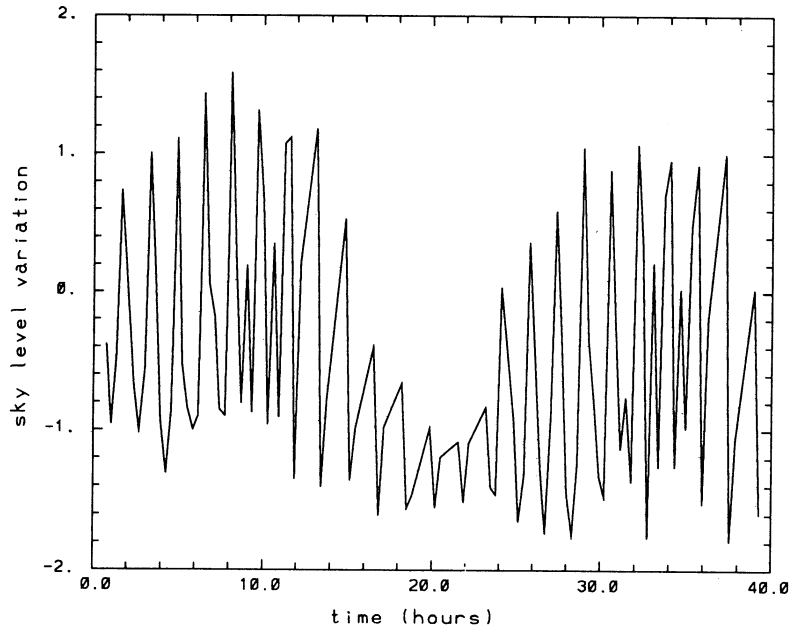

FIG. 7.—Modulation of background level in e^- per pixel (arbitrary zero point) as required to match the integrated intensity of all pixels within the image area after elimination of cosmic-ray events. This is treated as the measured sky level.

events. A most conservative estimate assuming the number of events grows with decreasing energy at the rate observed over 512 to $128e^-$ ($\times 1.08$ per factor of 2 drop), and starting from the number at $128e^-$ yield a spurious contribution to the sky of $0.2e^-$ per pixel. Assuming the extrapolation rate to be $\times 1.45$ per factor of 2 as for single pixel events in Windhorst et al. (1994) yields a sky contribution of $0.7e^-$. The pyramid-shadowed region showed a larger event rate at $64e^-$; if this is real (it may be biased upward by ordinary Poisson fluctuations on the readout noise), then estimates of $1–2e^-$ per pixel, i.e., the full level indicated in Figure 7, are possible.

Another approach to estimating the real sky background relies on models of the sky brightness as a function of orbital geometry. Figure 8 shows the predicted sky background variation. Because the observations were obtained while 47 Tuc was in the CVZ of *HST*, the line of sight was relatively close to the limb of Earth for a substantial portion of each spacecraft orbit (the angle varied between 11° and 36°), although the near limb was not always illuminated by sunlight. Significant Earth light can be scattered from the interior of the Optical Telescope Assembly and the primary mirror into the telescope focal plane in that circumstance. However, ultraviolet observations are less affected than are longer wavelength observations because the UV albedo of Earth is 10 times less than the visible light albedo (Meier 1991). To assess the effect of scattered light in our observations, we computed the detected background light

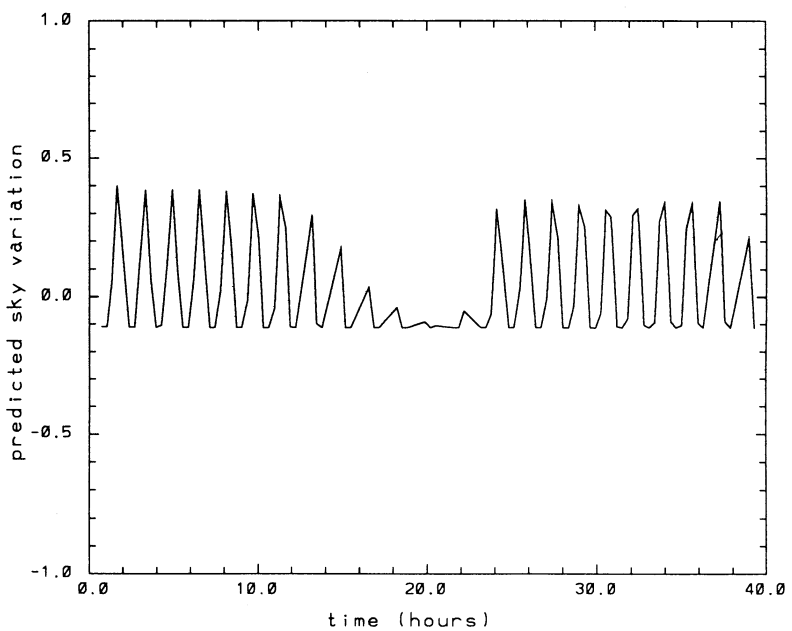

FIG. 8.—Predicted level of sky variation in e^- per pixel (arbitrary zero point) based on model of scattered Earth light into the *HST* focal plane

for each of the 99 observations. A scattered light computer code (Elkin 1994) which incorporates an angular integration of the optical telescope assembly–scattered terrestrial illumination during an exposure as well as the direct zodiacal background was utilized to compute the focal plane spectrum of scattered light incident on the WF/PC entrance aperture. The STSDAS SYNPHOT task was used to compute the instrumental response to that incident spectrum. The results are shown in Figure 8. Most of the observations were affected only by direct zodiacal light background, which does not vary during an orbit of the spacecraft. The remaining observations had backgrounds which were increased over the zodiacal background by no more than 50%. However, in all observations the computed zodiacal and scattered earthshine background was insignificant since it contributed no more than $0.5e^-$ to the measured signals. The peaks in Figure 8 occur at the *HST* orbital period and phase perfectly with peaks attributed to orbital modulation in Figure 5. The phasing of variations in Figure 8 are probably quite reliable, although one could question the computed amplitude.

We have attempted an independent empirical calibration of the time-variable background. A bilinear regression fit of the measured sky (Fig. 7) against the cosmic-ray rate (Fig. 5) and predicted sky level (Fig. 8) suggests that the peak-to-peak amplitude contributions should be $0.8e^-$ from real sky (assuming the model shape) and $2.0e^-$ from missed cosmic-ray events; this two-component fit represents the measured sky modulation to an rms of $0.2e^-$ (linear correlation of data and model is 0.97). The amplitudes of the two components estimated from the regression are in good accord with the independently estimated amplitudes, as presented above.

We have subtracted the sky variation as shown in Figure 7 from the individual data frames, although at this level sky modulation would be a minor contributor to the error budget for the stellar intensity estimates. At F336W the intrinsic sky background over 1000 s integrations was modulated by less than one electron during any orbit in the CVZ.

3.6. *Intensity Extractions*

Here we briefly discuss the approach to estimating intensities for individual stars over the time series of 99 frames. The cosmic-ray elimination work provided accurate (to about 0.01 pixel) relations between sky position and its corresponding x, y projection in CCD coordinates for all frames. We rely on DAOPHOT (Stetson 1987) for detection of all stars of interest using the mean F336W image oversampled by a factor of two as discussed in § 3.4. Returned positions for the 25 fiducial stars already used to derive the image-CCD offsets are used to transform the oversampled mean image coordinates to those appropriate to individual time series frames. *Therefore the intensity extractions assume that an accurate x, y position for all stars of interest are separately known for each data frame.*

We have previously addressed determination (and subtraction of) a small variable, but spatially uniform sky component. An accurate estimate of local sky in this data set would be very difficult. For our purposes it is sufficient to select a reasonable estimate of the sky level and demand that whatever local sky is used remain fixed across the full time series. We chose local sky for each star such that the ratio of encircled energies at radii of 2, 3, and 4 pixels match expected curves of growth for the PSF (bright, isolated stars on each chip are used to determine the expected curves of growth) averaged over all frames in the time series. Having determined the time-invariant estimate of local sky, this is then presubtracted from a region larger than any aperture to be used before extracting digital aperture sums or performing PSF fitting on individual stars. This sky value will also be of use in comparing realized time-series variances to model estimates of expected S/N.

We have used both digital aperture sums (with partial pixel sums to specified radii from the stellar center) and PSF fitting. The PSF adopted is

$$f(r) = ce^{(r/\sigma)^{-0.5}}, \quad (4)$$

where r is the distance (based on sum of squares of x, y distances) from the PSF center, σ is a scale length solved for on each frame (typical value ~ 0.21 pixel), and c is a normalization such that the sum to infinity equals unity. Partial pixel sums with (linear) oversampling of 20 (central 5 pixels), 9 (pixels 6–21) and 3 (pixels 22–69) in a radially growing sense are used to numerically fix $f(r)$ for any pixel. The PSF fits usually include 37 pixels. *We make no claim that this is an optimal theoretical PSF for fitting the cores of PC images*; it does, however, generate a decent match to the real PSF core and provides stable time series results.

4. OVERVIEW OF TIME SERIES PROPERTIES

4.1. *S/N and Detection Limits*

To qualify our intensity extraction techniques to be applied to some 20,000 stars we start with a detailed consideration of results for a more manageable subset of 50 stars on PC6 spanning the full brightness range to be considered. These stars were selected by visual inspection of the oversampled image and will be representative of the full set with an acknowledged bias to well-isolated cases. Edmonds et al. (1995) will discuss the range of characteristics (e.g., effects of close neighbors) that arise in the full ensemble.

We have previously defined the variation of x and y image motion and sky background that influence our approach to data analyses and may also introduce correlated noise into the time series. Figure 9 shows two additional measures of image changes through the time series. The PSF scale factor is σ from equation (4) and may be thought of as a seeing-like parameter. Variation of the PSF scale is presumably induced by small changes in telescope focus resulting from changes of the thermal balance of the optical telescope assembly. Also shown in Figure 9 are the frame-to-frame variations of intensity (normalized to unity) averaged over the 25 bright, well-isolated stars. The digital aperture sums (radius of 4 pixels) demonstrate remarkable stability—the standard deviation is only 0.2% (2 mmag in photometric terms). The total count rates per frame are $\sim 1.6 \times 10^8 e^-$ from stellar sources, $\sim 5 \times 10^6 e^-$ from cosmic rays (3.0% of total, but modulated from 2% to 4.5%) and a modulated sky (peak-to-peak) level of $\sim 1.6 \times 10^6 e^-$ (from real sky and undetected cosmic rays). *The aperture sums suggest that any instrumental sensitivity changes are below the level of* 0.2% *which is small compared to the S/N attainable for any single star* and is small compared to "sky" variations ($\sim 1\%$). The intensity estimates from PSF fitting are obviously fluctuating in step with the PSF scale changes as caused by telescope "breathing." The PSF mean intensity time series shows a standard deviation of 1.6% and shows a linear correlation with the PSF scale fluctuations > 0.99. Although the variations of PSF-based intensities are large, the same frame-to-frame "mistake" will be made for *all* stars. Differential time series photometry of any single star is derived by normalization to the ensemble mean (Gilliland et al. 1991) of

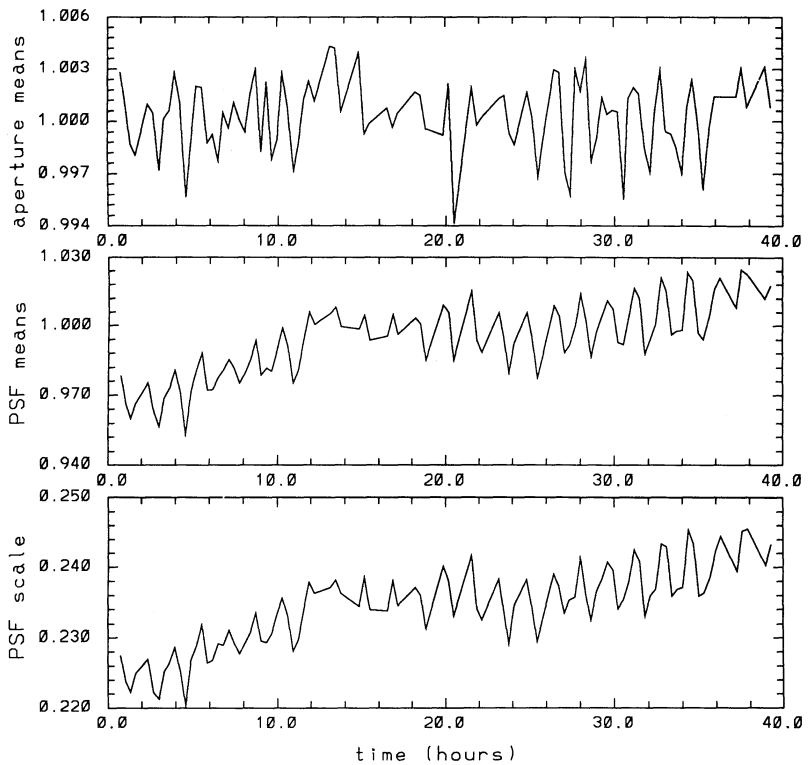

FIG. 9.—The upper panel shows the mean intensity averaged over 25 bright, nonvariable stars on PC6 (with arbitrary normalization to unity near the midpoint of the time series) using digital aperture photometry with a radius of 4 pixels. The middle panel shows the same but for PSF fitting to 37 pixels on each star. The lower panel shows the change of PSF scale (see eq. [4]) derived from the PSF fits.

25 bright, nonvariable stars for which the intensities were extracted identically. After performing the ensemble normalization, PSF photometry is as precise as aperture photometry for the bright stars and should, through the ability to select an optimal pixel weighting function, provide better results on faint stars. Note that in the case of digital aperture photometry the near-constancy of the aperture means (Fig. 9, *top panel*) implies that ensemble normalization is not an important step in this case.

Figure 10 shows the distribution of relative time series rms for 50 stars spanning our bright and faint limits. The particular points plotted are for aperture photometry (radius of 3 pixels); the continuous curve is based on a simple error budget accounting only for Poisson statistics on the object and sky background and readout noise. That this simple error budget works well for faint stars, but underestimates errors for the bright stars, does not come as a surprise. Photometry for bright stars suffers from additional significant error terms: (1) Flat-field errors will exist in the range of perhaps 2% per pixel. Half of the (core) flux comes from just the central 9 pixels in the PSF. As shown in Figure 3 the intensity on any given pixel can be modulated at unit amplitude by x, y motions. Flat-field errors will lead to nonperfect cancellations of motion-induced fluctuations ($\sim 2\%/9^{1/2} \sim 0.007$) over the sum of several pixels. This term alone is probably sufficient to rationalize the higher errors on the bright stars. (2) Although with fits to individual position defining stars good to 0.024 pixel (rms), and with 25 such stars fixing the mean frame offset error to order 0.005 pixel, reference to Figure 3 suggests that even this small error in predicting the position of a given star may induce frame-to-frame errors at a few parts per thousand on the intensity estimates.

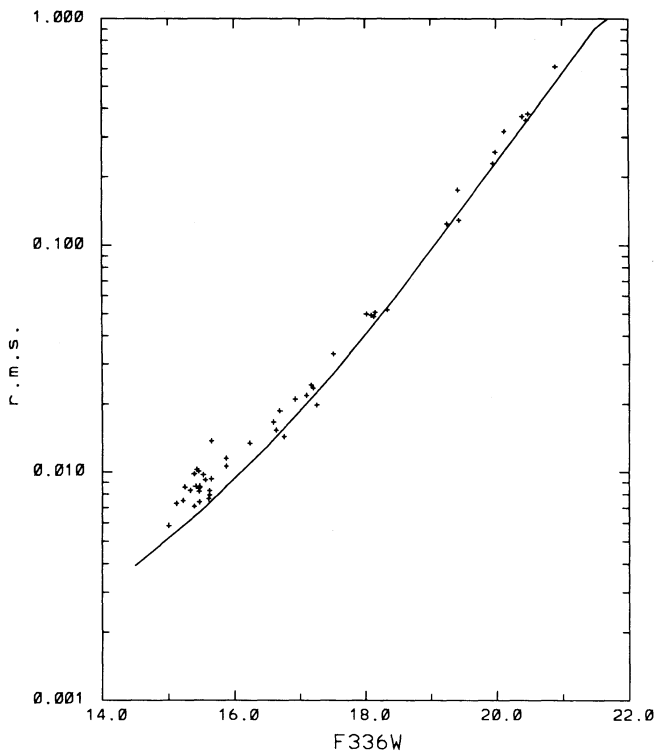

FIG. 10.—Distribution of time series standard deviations vs. apparent magnitude in the F336W ($\approx U$) filter for 50 stars spanning the intensity range of interest. Aperture photometry with a radius of 3 pixels was used. The solid curve is a model for the error budget assuming only Poisson statistics on the object and background and CCD readout noise.

The error budget assumes a readout noise of $15e^-$ and a typical "sky" (i.e., PSF halo) background brightness of $170e^-$. For an aperture of radius equal to 2 pixels, reaching a S/N of 2 requires $143e^-$ ($\sim$20 DN) within the aperture from the stellar PSF. About 20% of the $r = 2$ aperture sum will fall on the central pixel; therefore our useful time series photometry limit occurs for stars with a peak intensity above background of about 4 DN, or $30e^-$. With 99 points in the time series, our sensitivity to detection (assume 4 σ confidence) of coherent oscillations is about 0.4 times the time series rms (Scargle 1982). Adopting the faint limit of S/N = 2 per frame implies a coherent oscillation detection limit (half-amplitude) of about 0.2 mag. At the bright end of the stellar ensemble a time series rms of 5 mmag is reached in the best cases implying that oscillations with amplitudes down to 2 mmag should be detectable. (Actually the best time-series rms reaches 3–4 mmag on bright stars which tend to have better precisions with use of larger apertures; the use of $r = 2$ or 3 is optimal only for the faint stars.) Therefore on the brightest blue stragglers for which $m_U \sim 15$, even very low amplitude δ Scuti oscillations are detectable. At the faint limit of $m_U \sim 21$ ($M_U \sim 7.7$) we have useful sensitivity to detection of orbital modulation of possible cataclysmic variables.

4.2. *Common Time-Series Artifacts*

In § 2.2 and Figure 3 we documented the problems associated with imperfect *HST* guiding on the cosmic-ray elimination process. Individual pixels in PSF cores experience intensity modulations of order unity on both the *HST* orbital period and a long-term drift. Any CCD or calibration defect near a stellar-PSF core will lead to imperfect cancellation of the image motion signal. Figure 11 shows the image-CCD position offset time series for the motion in y, the PSF scale change, and the corresponding intensity (this is after summing over a full aperture and after normalizing to the mean intensity of 25 nonvariable stars, i.e., not just a single pixel as illustrated in Fig. 3) for a star on PC5 at $(x, y) = (275, 406)$. The external parameters and intensity time series power spectra show peaks at both the *HST* orbital frequency and at low frequency from the slow drift. This will be a general (albeit not universal) characteristic of apparently significant stellar variations that in fact are more likely artifacts: the power spectra show characteristic peaks at both low and *HST* orbital frequencies. The most common cause of such artifacts is a pixel-to-pixel flat-field error causing imperfect cancellation of signals such as that illustrated in Figure 3. Other external variations (e.g., modulation of PSF scale) show similar combinations of both low- and orbital-frequency changes. The fluctuating sky background shown in Figure 7 does not have a significant low-frequency component, but even for a faint star at the S/N = 2 limit (see § 4.1), an error at unit amplitude in subtraction of this term would add insignificantly to the error budget and the resulting (spurious) power spectrum components would remain well under the quoted detectability level for coherent oscillations.

Apparent stellar signals that reflect the orbital- and low-frequency variations associated with image motion and PSF scale changes will always be attributed to artifacts and discounted. These spurious time series signals could be removed, or substantially decreased, by decorrelation against the forcing external parameters. As argued by Gilliland et al. (1991) decorrelation works well if high-frequency (compared to the full data window) signals are in question and if hundreds of data points are available. In the current case we are interested in stellar signals at relatively low frequency, and with only 99 points in

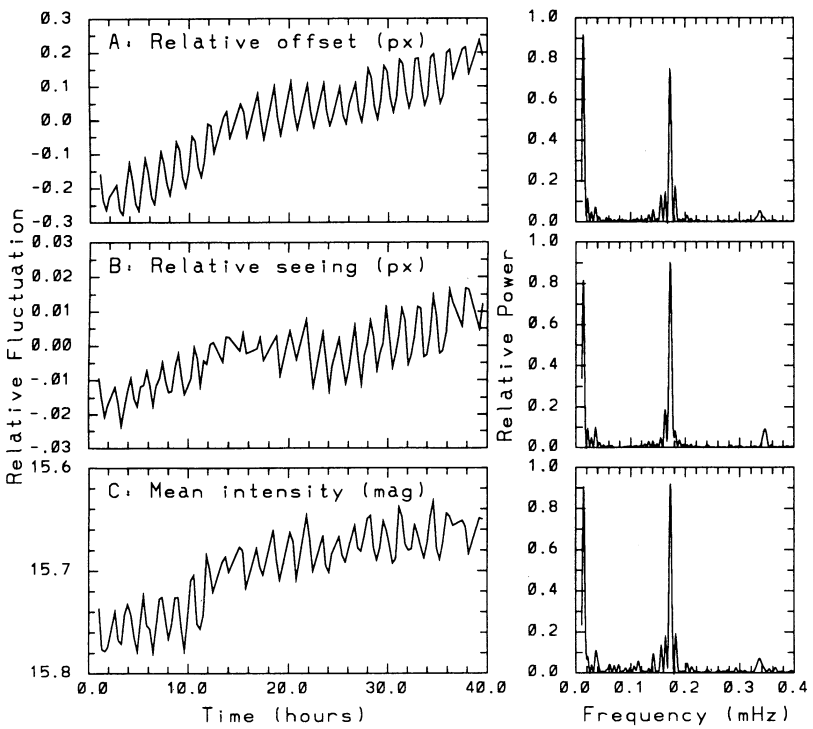

FIG. 11.—Example of time series showing apparent variation that is a simple artifact of the image x, y motion and CCD defects. Panel (*a*) shows the y motion of image position vs. CCD coordinates. Panel (*b*) shows the PSF scale change (σ from eq. [4]). Panel (*c*) shows the stellar intensity time series as derived from aperture photometry. Left-hand panels show direct time series, and right-hand panels are the respective power spectra showing nearly identical features in the stellar and external parameter temporal variations; note in particular the strong *HST* orbital peak at 0.17325 mHz.

the time series, indiscriminate application of decorrelation would sometimes remove real stellar signals. We do not therefore routinely invoke decorrelation against x, y motion and PSF scale change vectors for the time series processing, although in special cases this will be useful to consider. The purpose of this example is to point out that certain classes of apparent variation should not be accepted as stellar in origin given the ready explanation in terms of CCD artifacts coupled with image-CCD position changes. Ensemble normalization against the mean intensity of a group of nonvariable stars is a form of decorrelation; in this case the forcing function is assumed to apply equally to all stars (verified to be true) and it is always a valid processing step. Induced signals from x, y motions and PSF scale changes require existence of associated problems, e.g., a flat-field error on a contributing pixel, and therefore the amplitude of the effect may vary strongly for different stars.

4.3. *Examples of Detections*

In this section we show light curves for a few of the variable stars detected in the center of 47 Tucanae. Our temporal sampling and precision levels yield excellent sensitivity to δ Scuti oscillations, contact binaries and eclipsing binaries. Figure 12 shows the intensity variation and resulting power spectra for the following: Figure 12*a*: A blue straggler (based on our preliminary colors) with δ Scuti (or SX Phe) oscillations (from PC6 at $i, j = 392, 135$). The two detected modes have frequencies of 0.1135, 0.1470 mHz, or periods of 2.447, and 1.890 hr, respectively. The period ratio of 0.772 ± 0.001 falls within the narrow range (0.768–0.778) expected for δ Scuti stars of Population II oscillating in the fundamental and first overtone modes (Peterson & Jørgensen 1972). Figure 12*b*: A near-contact binary system with a period of 10.40 ± 0.05 hr (from PC6 at $i, j = 468, 250$). Figure 12*c*: A faint eclipsing binary with a period of 26.4 ± 0.3 hr (from PC6 at $i, j = 691, 517$). These stars do not show any excess power at the *HST* orbital frequency; this is true for most stars, whether variable or not. Proper astrophysical interpretation of these and other detected variables will appear in subsequent papers in this series. Gilliland et al. (1995) will discuss the blue straggler population in which several δ Scuti and W UMa binary oscillators are detected. Consistency checks on membership, cluster distance modulus, and physical characteristics of the variable stars can be obtained for both W UMa (Rucinski 1994) and δ Scuti (Nemec, Linnell Nemec, & Lutz 1994) variables by comparison with calibrated period-luminosity relations. Edmonds et al. (1995) will discuss the general frequency of close binary systems, including a full discussion of completeness. These further interpretations will require analysis of absolute photometry in U, B, and V—a topic generally distinct from the differential photometry techniques discussed in this paper.

5. DISCUSSION

We have introduced a unique set of *HST* data that supports definitive searches for several types of stellar variability in the population of stars at the center of 47 Tucanae. Acquisition of the data required development of procedures for and utilization of the continuous viewing zone for *HST*. The combination of undersampled images and frame-to-frame guiding errors pose a difficult problem for elimination of cosmic-ray events, which if left untreated would dominate the time series error budgets. Our technique of detecting and eliminating cosmic rays under these conditions was shown to work very well in support of time series photometry, and the technique has general relevance to high-resolution imaging applications. The derived time series have errors well characterized by

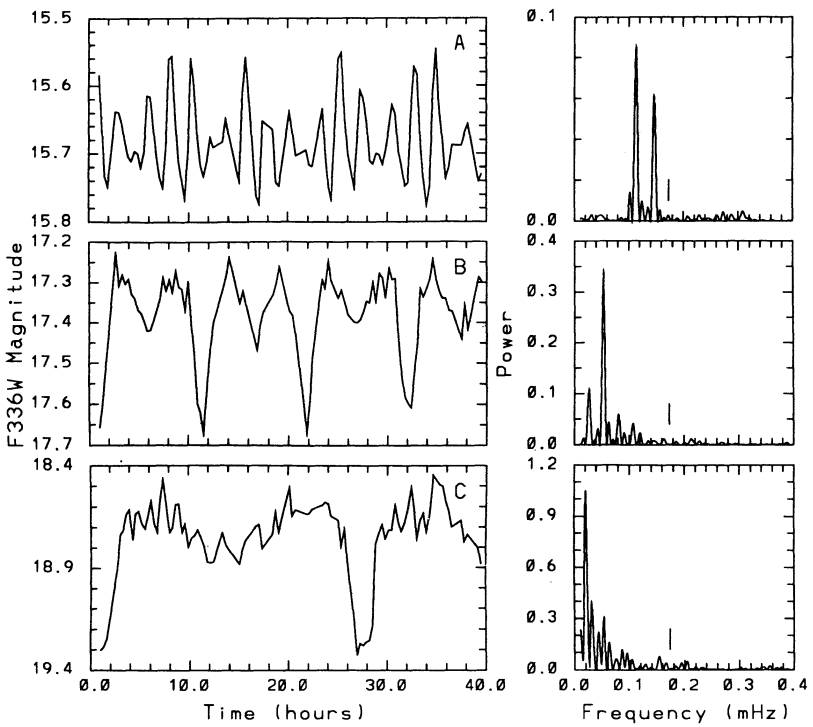

FIG. 12.—Examples of variable stars detected in the central region of 47 Tucanae. Magnitudes are for F336W ($\approx U$). Panel (*a*) shows a blue straggler with double mode δ Scuti (or SX Phe) oscillations. A near-contact binary system is shown in (*b*). Panel (*c*) shows an eclipsing binary. A tick mark placed at the *HST* orbital frequency (0.17325 mHz) in each power spectrum shows where excess power might occur; all of these stars are free from the effect illustrated in Fig. 11.

expected terms from CCD readout noise, Poisson fluctuations on the target and background level, and for the brighter targets flat-field errors also contribute. Classic examples of δ Scuti, near-contact, and eclipsing binary systems have been identified in the time series.

This project will provide a definitive search for variations of either δ Scuti or W UMa type on the blue stragglers at the center of 47 Tuc. Significant observational gains at defining time series for these stars would be very difficult. In a similar vein our temporal sampling, both integration times and length of the full time series, is well matched to the detection of W UMa and short-period eclipsing binary systems in the general stellar population. Except for W UMa systems well down the main sequence in 47 Tuc our observations should provide good completeness and light curve characterization. Significant gains could be made with WFPC2 observations for photometry on the faint stars for which the spherical aberration–induced sky background and readout noise terms are much smaller. For detection of cataclysmic variables via orbital modulation, the current data set has very limited capabilities; a similarly extensive observation set with WFPC2 could provide definitive results for an expected cataclysmic variable population (Di Stefano & Rappaport 1994).

The authors would like to acknowledge the help of Vicki Balzano, Doug Van Orsow, Peggy Stanley, Conrad Sturch, and Bill Workman and many other dedicated individuals at the STScI in various aspects of scheduling this unique proposal. We acknowledge the encouragement of David Elkin, Riccardo Giacconi, and Nolan Walborn in efforts directed at making the Continuous Viewing Zone of *HST* a usable resource. In the area of data analysis we have benefited from discussions with Pierre Bely, Eddie Bergeron, John Biretta, Chris Burrows, Roberto Gilmozzi, and John Mackenty. We also acknowledge discussions of astronomy with Raja Guhathakurta, Mario Livio, Francesco Paresce, and Peter Stetson.

REFERENCES

Burrows, C. J., Holtzman, J. A., Faber, S. M., Bely, P. Y., Hasan, H., Lynds, C. R., & Schroeder, D. 1991, ApJ, 369, L21
De Marchi, G., Paresce, F., & Ferraro, F. R. 1993, ApJS, 85, 293
Di Stefano, R., & Rappaport, S. 1994, ApJ, 423, 274
Edmonds, P. D., et al. 1995, in preparation
Elkin, D. 1994, private communication
Fabian, A. C., Pringle, J. E., & Rees, M. J. 1975, MNRAS, 172, 15P
Gilliland, R. L., et al. 1991, AJ, 101, 541
Gilliland, R. L., et al. 1995, in preparation
Guhathakurta, P., Yanny, B., Schneider, D. P., & Bahcall, J. N. 1992, AJ, 104, 1790
Hertz, P., & Grindlay, J. 1983, ApJ, 275, 105
Hesser, J. E., Harris, W. E., Vandenberg, D. A., Allwright, J. W. B., Shott, P., & Stetson, P. B. 1987, PASP, 99, 739
Hills, J. G., & Day, C. A. 1976, Astrophys. Lett., 17, 87
Hut, P., McMillan, S., Goodman, J., Mateo, M., Phinney, S., Pryor, T., Richer, H., & Weinberg, M. 1992, PASP, 104, 981
Hut, P., McMillan, S., & Romani, R. W. 1992, ApJ, 389, 527
Manchester, R. N., Lyne, A. G., Robinson, C., D'Amico, N., Bailes, M., & Lim, J. 1991, Nature, 352, 219
Mateo, M. 1993, in Blue Stragglers, ed. R. A. Saffer (ASP Conf. Series, 53), 74
Mateo, M., Harris, H. C., Nemec, J., & Olszewski, E. W. 1990, AJ, 100, 469
Meier, R. R. 1991, Space Sci. Rev., 58, 1
Nemec, J. M., Linnell Nemec, A. F., & Lutz, T. E. 1994, AJ, 108, 222
Paresce, F. et al. 1991, Nature, 352, 297
Peterson, J. O., & Jørgensen, H. E. 1972, A&A, 17, 367
Rucinski, S. M. 1994, PASP, 106, 462
Scargle, J. D. 1982, ApJ, 263, 835
Shara, M. M., Drissen, L., Bergeron, L. E., & Paresce, F. 1995a, ApJ, 441, 617
Shara, M. M., et al. 1995b, in preparation
Stetson, P. B. 1987, PASP, 99, 191
Windhorst, R. A., Franklin, B. E., & Neuschaefer, L. W. 1994, PASP, 106, 798
Yan, L., & Mateo, M. 1994, AJ, 108, 1810